Investigation of coalescence-induced droplet jumping on superhydrophobic surfaces and liquid condensate adhesion on slit and plain fins

CrossMark

Y. Shi, G.H. Tang *, H.H. Xia

MOE Key Laboratory of Thermo-Fluid Science and Engineering, School of Energy and Power Engineering, Xi'an Jiaotong University, Xi'an 710049, China

ABSTRACT

The coalescence-induced droplet jumping on superhydrophobic complex textured surface, as well as the liquid condensate adhesion on slit and plain fins with hydrophobic and hydrophilic coatings in the tube-and-fin heat exchanger is studied numerically using the three-dimensional multi-relaxation-time (MRT) pseudopotential lattice Boltzmann model. It is found that the height of the surface conical posts, the spacing between the consecutive conical posts, the number of the droplets, the radius of the droplet, and the wettability property of the complex textured surface have important effect on the spontaneous jumping of the coalesced droplet. For the liquid condensate adhesion on slit and plain fins, it is found that both the hydrophilic coating with small contact angle and the hydrophobic coating with large contact angle are effective on avoiding liquid bridge between fins. Furthermore, the coating is required more strictly for slit fin than for plain fin to avoid liquid bridge.

© 2015 Elsevier Ltd. All rights reserved.

1. Introduction

Dropwise condensation behavior plays significant role in engineering applications, such as heat exchangers, air conditioners, thermal management, etc. When the droplets coalesce on a super-hydrophobic surface (the contact angle between liquid and surface exceeds 150°), the coalesced droplet can jump spontaneously from the surface due to the released excess surface energy [1]. If the shape and the wettability property of the textured surface are designed properly, the coalesced droplet can not only jump from the textured surface easily but also enhance the heat transfer performance, which is widely used in the applications of self-cleaning, microfluidics, and lab-on-chip devices. Recently, more and more studies have been focusing on the spontaneous jumping of coalesced droplet on superhydrophobic surfaces during dropwise condensation [2,3]. Peng et al. [3] experimentally observed the properties of the coalesced droplet induced by the coalescence of two droplets with the same volume and used the two-dimensional free energy lattice Boltzmann model to simulate the droplet coalescence process. Nam et al. [4] found that

approximately half of the excess surface energy released during the coalescence is efficiently converted to kinetic energy on the superhydrophobic surface before the detachment process. Liu et al. [5] used two-dimensional lattice Boltzmann method to simulate the droplet self-propelled jumping on superhydrophobic surfaces. Wang et al. [6] established the relation among the coalescence-induced velocity, surface energy, viscous dissipation, and droplet size without consideration of gravity.

The tube-and-fin heat exchanger is commonly applied in refrigeration, air-conditioner, and humidifier system. However, the liquid bridge forms easily between the adjacent fins with small spacing. Liquid condensate adhesion on fins may increase the pressure drop and deteriorate the heat transfer performance. Furthermore, the water condensate may corrode fins, produce corrosion, and cause superfluous noise [7]. Sommers et al. [8] showed that the anisotropic micro-grooved structure of the fin surface in combination with an alkyl silane coating can reduce liquid retention by more than 27%. Guo et al. [9] obtained stable biomimetic superhydrophobic surfaces on aluminum alloy using wet chemical etching followed by modification of the surface with a cross-linked silicone elastomer, perfluorononane (C_9F_{20}) and perfluoropolyether (PFPE). Shin et al. [10] found that the water hold-up in a heat exchanger could be reduced by the enhancement of the surface hydrophilicity and the design with lower number of fins.

Although researchers have numerically investigated the spontaneous droplet jumping on the textured surface and the different wettability coatings of the tube-and-fin surface, most of them simulated the spontaneous droplet jumping from two-dimensional point of view and the textured surface is simple [3,5,6]. The three-dimensional (3D) numerical simulations about the geometry and the wettability property of the complex textured surface for spontaneous jumping of the coalesced droplet, as well as the different wettability coatings of the tube-and-fin surface for the liquid condensate adhesion are still lacking. In the present work, we aim to investigate the coalescence-induced droplet jumping on superhydrophobic complex textured surfaces and to simulate the liquid condensate adhesion on slit and plain fins with hydrophobic and hydrophilic coatings in tube-and-fin heat exchanger using the 3D MRT pseudopotential lattice Boltzmann method. To the authors' best knowledge, there is no one using the 3D MRT pseudopotential lattice Boltzmann model to study the spontaneous droplet jumping on the complex textured surface, especially for the curved solid boundary, as well as the liquid condensate adhesion on slit and plain fins. The present work fills a gap in the literature by demonstrating that the three-dimensional MRT pseudopotential lattice Boltzmann method is effective to simulate the coalescence-induced droplet jumping on the complex textured surface and investigate the liquid condensate adhesion on slit and plain fins. The results can also be helpful to understand the processes involved with droplet in engineering applications of enhanced heat transfer.

Because the lattice Boltzmann method (LBM) is naturally suitable for massively parallel computation, this method can be used for large-scale simulations of complex fluids in various specific cases and boundary conditions [11–15]. The pseudopotential model, also known as the Shan–Chen (SC) model, is one of the most widely used and successful outgrowths of lattice Boltzmann models for multiphase flows. In this model, a density-dependent interparticle potential is employed to mimic the intermolecular interactions which separate phases in real fluids. Consequently the computational cost is reduced. Moreover, different wetting properties can be easily obtained just by tuning the interaction strength between the fluid and solid wall [16] and different equations of state (EOS) can also be easily incorporated [17]. However, this model also suffers from several drawbacks such as large spurious currents and thermodynamic inconsistency. Such deficiencies lead to numerical instability and put severe limitations on its application. To overcome this problem many researchers improved the pseudopotential model significantly. Shan [18] proposed a method of highly isotropic gradient operators to reduce the spurious currents. Sbragaglia et al. [19] developed the multirange pseudopotential model which moves the spatial range of the pseudopotential interactions to the next-nearest-neighbor lattice site. Li et al. [20] improved the forcing scheme of the two-dimensional pseudopotential lattice Boltzmann model to achieve thermodynamic consistency and large density ratio.

The rest of this paper is organized as follows. Firstly, a brief introduction is given to the three-dimensional MRT pseudopotential lattice Boltzmann model. Secondly, the three-dimensional MRT pseudopotential lattice Boltzmann model is validated with two tests. Thirdly, the coalescence-induced droplet jumping on superhydrophobic complex textured surfaces and the liquid condensate adhesion on slit and plain fins of fin-and-tube heat exchanger for different wettability coatings are investigated. Finally, a brief conclusion is drawn.

2. Three-dimensional MRT pseudopotential lattice Boltzmann model

The multi-relaxation-time method is able to improve numerical stability and reduce the spurious velocity by tuning the adjustable relaxation parameters [21]. In this article, the three-dimensional nineteen-velocity (D3Q19) lattice Boltzmann model with MRT collision operator is considered. The evolution equation of the D3Q19 lattice Boltzmann model with MRT collision operator can be written in a more general form as [22]

$$f_\alpha(\mathbf{x} + \mathbf{e}_\alpha \delta_t, t + \delta_t) = f_\alpha(\mathbf{x}, t) - \sum_\beta \mathbf{\Omega}_{\alpha\beta}(f_\beta(\mathbf{x}, t) - f_\beta^{eq}(\mathbf{x}, t))$$
$$+ S_\alpha(\mathbf{x}, t) - \frac{1}{2}\sum_\beta \mathbf{\Omega}_{\alpha\beta} S_\beta(\mathbf{x}, t) \tag{1}$$

where $f_\alpha(\mathbf{x}, t)$ is the density distribution function, $\mathbf{x}$ is the spatial position, and $\mathbf{e}_\alpha$ ($\alpha = 0, 1, \ldots 18$) is the discrete velocity along the αth direction given by

$$[\mathbf{e}_0, \mathbf{e}_1, \ldots, \mathbf{e}_{18}] = \begin{bmatrix} 0 & 1 & -1 & 0 & 0 & 0 & 0 & 1 & 1 & -1 & -1 & 1 & -1 & 1 & -1 & 0 & 0 & 0 & 0 \\ 0 & 0 & 0 & 1 & -1 & 0 & 0 & 1 & -1 & 1 & -1 & 0 & 0 & 0 & 0 & 1 & 1 & -1 & -1 \\ 0 & 0 & 0 & 0 & 0 & 1 & -1 & 0 & 0 & 0 & 0 & 1 & 1 & -1 & -1 & 1 & -1 & 1 & -1 \end{bmatrix} \tag{2}$$

$S_\alpha(\mathbf{x}, t)$ is the forcing term in the velocity space written as [23].

$$S_\alpha(\mathbf{x}, t) = w_\alpha \left[\frac{\mathbf{e}_\alpha - \mathbf{u}}{c_s^2} + \frac{\mathbf{e}_\alpha \cdot \mathbf{u}}{c_s^4} \mathbf{e}_\alpha \right] \cdot \mathbf{F} \tag{3}$$

where $w_0 = 1/3$, $w_\alpha = 1/18$ for $\alpha = 1 - 6$ and $w_\alpha = 1/36$ for $\alpha = 7 - 18$. $\mathbf{F}$ is the total force on each particle, including the fluid–fluid force $\mathbf{F}_f$, the fluid–solid interaction force $\mathbf{F}_s$ and the body force $\mathbf{F}_b$. $\mathbf{\Omega}_{\alpha\beta}$ is the collision matrix in the velocity space. Eq. (1) is projected to moment space by the transformation matrix $\mathbf{M}$. Thus, Eq. (1) can be transformed to the following form

$$f_\alpha(\mathbf{x} + \mathbf{e}_\alpha \delta_t, t + \delta_t) = f_\alpha(\mathbf{x}, t) - \mathbf{M}^{-1}\mathbf{\Lambda}(\mathbf{m}(\mathbf{x}, t) - \mathbf{m}^{eq}(\mathbf{x}, t))$$
$$+ \mathbf{M}^{-1}\left(\mathbf{I} - \frac{\mathbf{\Lambda}}{2}\right)\bar{\mathbf{S}}(\mathbf{x}, t) \tag{4}$$

where the transformation matrix $\mathbf{M}$ for the D3Q19 lattice model is given by

$$\mathbf{M} = \begin{bmatrix}
1 & 1 & 1 & 1 & 1 & 1 & 1 & 1 & 1 & 1 & 1 & 1 & 1 & 1 & 1 & 1 & 1 & 1 & 1 \\
-30 & -11 & -11 & -11 & -11 & -11 & -11 & 8 & 8 & 8 & 8 & 8 & 8 & 8 & 8 & 8 & 8 & 8 & 8 \\
12 & -4 & -4 & -4 & -4 & -4 & -4 & 1 & 1 & 1 & 1 & 1 & 1 & 1 & 1 & 1 & 1 & 1 & 1 \\
0 & 1 & -1 & 0 & 0 & 0 & 0 & 1 & -1 & 1 & -1 & 1 & -1 & 1 & -1 & 0 & 0 & 0 & 0 \\
0 & -4 & 4 & 0 & 0 & 0 & 0 & 1 & -1 & 1 & -1 & 1 & -1 & 1 & -1 & 0 & 0 & 0 & 0 \\
0 & 0 & 0 & 1 & -1 & 0 & 0 & 1 & 1 & -1 & -1 & 0 & 0 & 0 & 0 & 1 & -1 & 1 & -1 \\
0 & 0 & 0 & -4 & 4 & 0 & 0 & 1 & 1 & -1 & -1 & 0 & 0 & 0 & 0 & 1 & -1 & 1 & -1 \\
0 & 0 & 0 & 0 & 0 & 1 & -1 & 0 & 0 & 0 & 0 & 1 & 1 & -1 & -1 & 1 & 1 & -1 & -1 \\
0 & 0 & 0 & 0 & 0 & -4 & 4 & 0 & 0 & 0 & 0 & 1 & 1 & -1 & -1 & 1 & 1 & -1 & -1 \\
0 & 2 & 2 & -1 & -1 & -1 & -1 & 1 & 1 & 1 & 1 & 1 & 1 & 1 & 1 & -2 & -2 & -2 & -2 \\
0 & -4 & -4 & 2 & 2 & 2 & 2 & 1 & 1 & 1 & 1 & 1 & 1 & 1 & 1 & -2 & -2 & -2 & -2 \\
0 & 0 & 0 & 1 & 1 & -1 & -1 & 1 & 1 & 1 & 1 & -1 & -1 & -1 & -1 & 0 & 0 & 0 & 0 \\
0 & 0 & 0 & -2 & -2 & 2 & 2 & 1 & 1 & 1 & 1 & -1 & -1 & -1 & -1 & 0 & 0 & 0 & 0 \\
0 & 0 & 0 & 0 & 0 & 0 & 0 & 1 & -1 & -1 & 1 & 0 & 0 & 0 & 0 & 0 & 0 & 0 & 0 \\
0 & 0 & 0 & 0 & 0 & 0 & 0 & 0 & 0 & 0 & 0 & 0 & 0 & 0 & 0 & 1 & -1 & -1 & 1 \\
0 & 0 & 0 & 0 & 0 & 0 & 0 & 0 & 0 & 0 & 0 & 1 & -1 & -1 & 1 & 0 & 0 & 0 & 0 \\
0 & 0 & 0 & 0 & 0 & 0 & 0 & 1 & -1 & 1 & -1 & -1 & 1 & -1 & 1 & 0 & 0 & 0 & 0 \\
0 & 0 & 0 & 0 & 0 & 0 & 0 & -1 & -1 & 1 & 1 & 0 & 0 & 0 & 0 & 1 & -1 & 1 & -1 \\
0 & 0 & 0 & 0 & 0 & 0 & 0 & 0 & 0 & 0 & 0 & 1 & 1 & -1 & -1 & -1 & -1 & 1 & 1
\end{bmatrix} \tag{5}$$

With the transformation matrix $\mathbf{M}$, the density distribution function f_α and its equilibrium distribution f_α^{eq} can be projected onto the moment space through $\mathbf{m} = \mathbf{M}f$ and $\mathbf{m}^{eq} = \mathbf{M}f^{eq}$. The equilibrium distribution functions $\mathbf{m}^{eq}$ in the moment space are given by

$$\mathbf{m}^{eq} = \left(\rho, -11\rho + \frac{19}{\rho}\left(j_x^2 + j_y^2 + j_z^2\right), 3\rho - \frac{11}{2\rho}\left(j_x^2 + j_y^2 + j_z^2\right), j_x, \right.$$
$$-\frac{2}{3}j_x, j_y, -\frac{2}{3}j_y, j_z, -\frac{2}{3}j_z, \frac{1}{\rho}\left(2j_x^2 - \left(j_y^2 + j_z^2\right)\right),$$
$$-\frac{1}{2\rho}\left(2j_x^2 - \left(j_y^2 + j_z^2\right)\right), \frac{1}{\rho}\left(j_y^2 - j_z^2\right),$$
$$\left.-\frac{1}{2\rho}\left(j_y^2 - j_z^2\right), \frac{1}{\rho}j_xj_y, \frac{1}{\rho}j_yj_z, \frac{1}{\rho}j_xj_z, 0, 0, 0\right)^T, \tag{6}$$

where $j_x = \rho u_x, j_y = \rho u_y$ and $j_z = \rho u_z$ are the momentum fluxes. $\mathbf{I}$ in Eq. (4) is the identity matrix and Λ is a diagonal matrix given by

$$\Lambda = diag(s_1, s_2, s_3, s_4, s_5, s_6, s_7, s_8, s_9, s_{10}, s_{11}, s_{12}, s_{13}, s_{14}, s_{15}, s_{16}, s_{17}, s_{18}, s_{19})$$
$$= diag(0, s_e, s_\varepsilon, 0, s_q, 0, s_q, 0, s_q, s_\upsilon, s_\pi, s_\upsilon, s_\pi, s_\upsilon, s_\upsilon, s_\upsilon, s_t, s_t, s_t) \tag{7}$$

whose elements represent the inverse of the relaxation time for the transformed distribution function $\mathbf{m}$ as it is relaxed to the equilibrium distribution function in the moment space, $\mathbf{m}^{eq}$.

In the present work, we set $s_e = 0.3$, $s_\varepsilon = 0.8$, $s_q = 1.2$, $s_\upsilon = 1.1$, $s_\pi = 1.2$ and $s_t = 1.8$. The three-dimensional MRT force scheme $\bar{\mathbf{S}}$ is given by

$$\bar{S}_0 = 0, \ \bar{S}_1 = 38(u_xF_x + u_yF_y + u_zF_z) + \frac{114\gamma\left(F_x^2 + F_y^2 + F_z^2\right)}{(1/s_2 - 0.5)\psi(\mathbf{x}, t)^2},$$

$$\bar{S}_2 = -11(u_xF_x + u_yF_y + u_zF_z),$$

$$\bar{S}_3 = F_x, \bar{S}_4 = -\frac{2}{3}F_x, \bar{S}_5 = F_y, \bar{S}_6 = -\frac{2}{3}F_y, \bar{S}_7 = F_z, \bar{S}_8 = -\frac{2}{3}F_z,$$

$$\bar{S}_9 = 4u_xF_x - 2(u_yF_y + u_zF_z), \bar{S}_{10} = -2u_xF_x + u_yF_y + u_zF_z,$$

$$\bar{S}_{11} = 2(u_yF_y - u_zF_z), \bar{S}_{12} = -(u_yF_y - u_zF_z),$$

$$\bar{S}_{13} = u_xF_y + u_yF_x, \bar{S}_{14} = u_yF_z + u_zF_y, \bar{S}_{15} = u_xF_z + u_zF_x,$$

$$\bar{S}_{16} = \bar{S}_{17} = \bar{S}_{18} = 0, \tag{8}$$

where γ is used to tune the mechanical stability condition with $\gamma = 0.3$ in this article.

The corresponding macroscopic fluid density and momentum in the velocity space can be obtained from the following equations:

$$\rho = \sum_{\alpha=0}^{18} f_\alpha, \ \rho\mathbf{u} = \sum_{\alpha=0}^{18} \mathbf{e}_\alpha f_\alpha + \frac{\delta_t}{2}\mathbf{F} \tag{9}$$

The force acting on the fluid $\mathbf{F}$ consists of the fluid–fluid force $\mathbf{F}_f$ [24]

$$\mathbf{F}_f(\mathbf{x}, t) = -G\psi(\mathbf{x}, t)\sum_{\alpha=0}^{18} w_\alpha \psi(\mathbf{x} + \mathbf{e}_\alpha\delta_t, t)\mathbf{e}_\alpha \tag{10}$$

the fluid–solid interaction force $\mathbf{F}_s$ [25]

$$\mathbf{F}_s(\mathbf{x}, t) = -G\psi(\rho(\mathbf{x}, t))\sum_{\alpha=0}^{18} w_\alpha \psi(\rho_w)\phi(\mathbf{x} + \mathbf{e}_\alpha\delta_t, t)\mathbf{e}_\alpha \tag{11}$$

and the body force $\mathbf{F}_b$ [23]

$$\mathbf{F}_b(\mathbf{x}, t) = \rho(\mathbf{x}, t)g \tag{12}$$

where g is the gravitational acceleration, and G is a parameter that controls the strength of the inter-particle force. The density of solid phase is ρ_w, i.e., $\psi(\rho_w) = \psi(\rho(\mathbf{x}_w))$. Different contact angles can be obtained by adjusting the parameter ρ_w. Actually, ρ_w is not really relevant to the true density of the solid phase, and it is a free parameter used here to tune different wall properties instead of the true density of solid phase [26]. w_α are the weights with $w_0 = 1/3$, $w_\alpha = 1/18$ for $\alpha = 1 - 6$ and $w_\alpha = 1/36$ for $\alpha = 7 - 18$. $\phi(\mathbf{x} + \mathbf{e}_\alpha\delta_t, t)$ is the indicator function, which is equal to 1 when $\mathbf{x}$ is in solid and equal to 0 when $\mathbf{x}$ is in fluid. $\psi(\mathbf{x}, t)$ is the effective mass which is a function of the local density and is determined by the equation of state [17]:

$$\psi(\mathbf{x}, t) = \sqrt{2(p - \rho c_s^2)/(c_s^2 G)} \tag{13}$$

where $c_s = c/\sqrt{3}$ is the lattice sound speed, and $c = \delta_x/\delta_t$ is the ratio between the lattice spacing δ_x and the time step δ_t. In this article, δ_x and δ_t are set to be unity.

In this work, the Peng–Robinson (P–R) equation of state is used, which provides the maximum density ratio while maintaining

small spurious currents around the interface. The P–R equation of state is given by [27]

$$p = \frac{\rho RT}{1 - b\rho} - \frac{a\rho^2 \kappa(T)}{1 + 2b\rho - b^2\rho^2} \qquad (14)$$

where $\kappa(T) = [1 + (0.37464 + 1.54226\omega - 0.26992\omega^2)(1 - \sqrt{T/T_c})]^2$ and ω is the acentric factor which equals to 0.344. $a = 0.45724R^2T_c^2/p_c$, and $b = 0.0778RT_c/p_c$, where a is the attraction parameter, and b is the volumetric or repulsion parameter [23]. T_c and p_c are critical temperature and critical pressure, respectively. Following Gong and Cheng [27], the parameters in the present work are set to $a = 2/49$, $b = 2/21$ and $R = 1$, which are applicable to any fluids in the lattice Boltzmann computations [28].

3. Model validation

Two tests are considered to validate the three-dimensional MRT pseudopotential lattice Boltzmann model. First, the problem of stationary droplet is employed to compare the analytical solution by the Maxwell construction with the LBM results. The lattice number of 192^3 is adopted and a spherical droplet with a radius of $r_0 = 30$ in lattice unit is initially placed at the center of the domain. The periodic boundary conditions are applied on all sides of the domain. The density field is initialized as [20]

$$\rho(x, y, z) = \frac{\rho_l + \rho_g}{2} - \frac{\rho_l - \rho_g}{2}$$
$$\times \tanh \left[\frac{2\sqrt{(x - x_0)^2 + (y - y_0)^2 + (z - z_0)^2} - r_0}{W} \right]$$
$$(15)$$

where the thickness of the interface is $W = 3$ in lattice unit. According to the relevant data [29], the critical parameters about water are $T_c = 647.1$ K, $\rho_c = 322$ kg m^{-3} and $p_c = 22.064$ MPa. As shown in Fig. 1, the LBM results agree well with the analytical solutions in both gas branch ($\rho/\rho_c < 1$) and liquid branch ($\rho/\rho_c > 1$). Under different temperature conditions, the simulation results are in good agreement with those given by the Maxwell construction. It is demonstrated that the three-dimensional MRT pseudopotential lattice Boltzmann model is capable of achieving thermodynamic consistency.

Another test is the Laplace law. From the Laplace's law, the pressure difference inside and outside a droplet of radius r is a
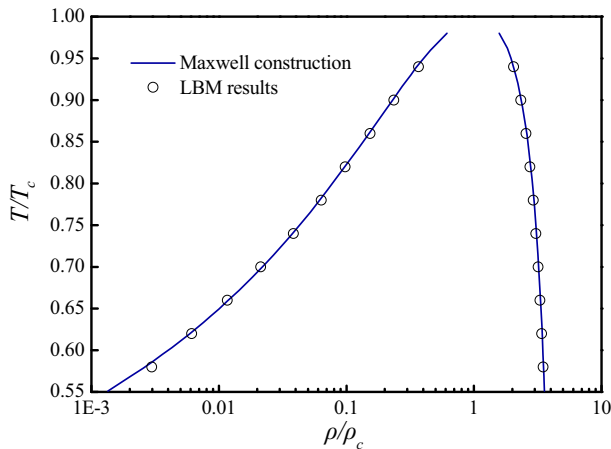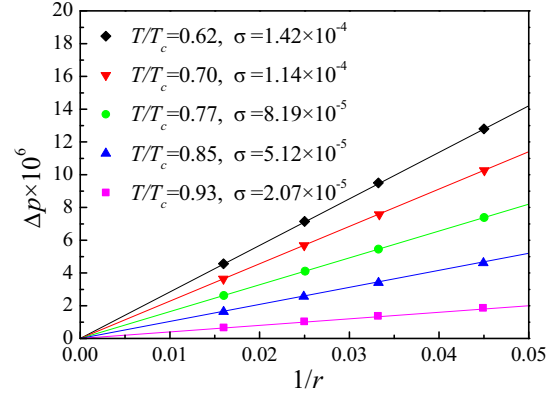

Fig. 2. Comparison of the LBM results (scatter symbols) with the Laplace's law (the solid lines) for pressure drop across a stationary droplet interface. Δp, σ and r are in lattice unit.

linear function of the inverse radius [30] with $\Delta p = 2\sigma/r$, where σ is the surface tension, and Δp represents the pressure difference. The relationship between Δp and $1/r$ at different temperatures and different surface tensions is presented in Fig. 2. When the temperatures are $T/T_c = 0.62$, $T/T_c = 0.70$, $T/T_c = 0.77$, $T/T_c = 0.85$ and $T/T_c = 0.93$, the surface tensions in lattice unit are $\sigma = 1.42 \times 10^{-4}$, $\sigma = 1.14 \times 10^{-4}$, $\sigma = 8.19 \times 10^{-5}$, $\sigma = 5.12 \times 10^{-5}$ and $\sigma = 2.07 \times 10^{-5}$, respectively. It can be seen that the model predictions are in excellent agreement with the Laplace's law. It indicates that the three-dimensional MRT pseudopotential lattice Boltzmann model can capture the phase interface correctly.

4. Results and discussion

4.1. Coalescence-induced droplet jumping on superhydrophobic surfaces

Study of the droplet behavior on rough surfaces is of great importance because almost all solid surfaces in nature and industrial applications are rough on the microscopic scale. Droplets may jump from the suitably designed superhydrophobic surfaces with
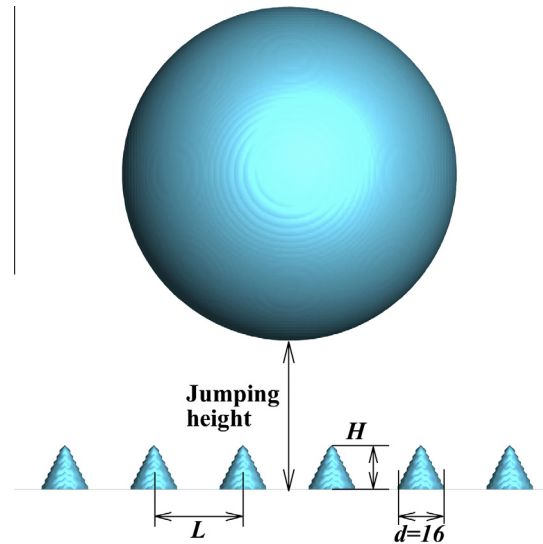

Fig. 3. Schematic diagram of the coalesced droplet jumping in 3D geometry. H is the height of the conical post, L is the distance between two consecutive conical posts, and $d = 16$ is the underside circle diameter of the conical post.

Fig. 1. Comparison of analytical solutions by the Maxwell construction with the LBM results.

the motion induced by the excess surface energy released during droplet coalescence. Such droplet jumping can offer further heat transfer enhancement over conventional dropwise condensation [2]. In this section, numerical simulations are carried out for the coalescence-induced droplet jumping on superhydrophobic complex textured surfaces.

The schematic diagram of the coalesced droplet jumping in 3D geometry is shown in Fig. 3. The simulation domain is $nx \times ny \times nz = 192 \times 192 \times 256$. In the following simulations, the parameters in lattice unit are fixed at density of liquid $\rho_l = 8.3$, density of gas $\rho_g = 4.15 \times 10^{-2}$, kinematic viscosity for both liquid and gas $\upsilon = 0.136$, surface tension $\sigma = 1.21 \times 10^{-4}$, temperature $T = 4.95 \times 10^{-2}$, and gravitational acceleration $g = 5 \times 10^{-6}$. No-slip boundary condition is applied on all the surfaces except for the complex textured surface. We use the scheme proposed by Bouzidi et al. [31] for the complex textured surface as schematic in Fig. 4. The parameter $q = |\mathbf{x}_f - \mathbf{x}_w|/|\mathbf{x}_f - \mathbf{x}_b|$ for $0 < q \leqslant 1$. Suppose that $\mathbf{x}_f$ is the fluid node, $\mathbf{x}_w$ is the wall node, and $\mathbf{x}_b$ is the solid node. Using quadratic interpolation we set
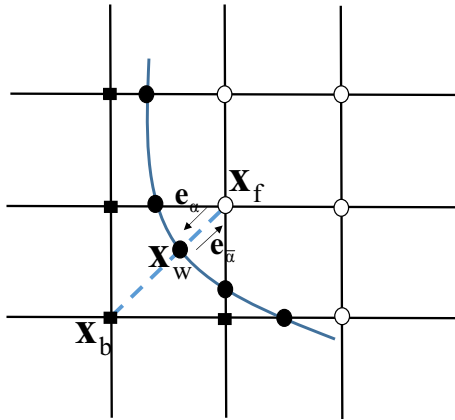

Fig. 4. Schematic diagram of Bouzidi scheme. The squares represent solid node, the filled circles represent boundary wall node, and the open circles represent fluid node.

$$f_{\bar{\alpha}}(\mathbf{x}_f, t + \delta_t) = q(1 + 2q)f_{\alpha}^+(\mathbf{x}_f, t) + (1 - 4q^2)f_{\alpha}^+(\mathbf{x}_f - \mathbf{e}_{\alpha}\delta_t, t)$$
$$- q(1 - 2q)f_{\alpha}^+(\mathbf{x}_f - 2\mathbf{e}_{\alpha}\delta_t, t), \quad q < \frac{1}{2} \qquad (16)$$

$$f_{\bar{\alpha}}(\mathbf{x}_f, t + \delta_t) = \frac{1}{q(1 + 2q)}f_{\alpha}^+(\mathbf{x}_f, t) + \frac{2q - 1}{q}f_{\bar{\alpha}}^+(\mathbf{x}_f, t)$$
$$+ \frac{1 - 2q}{1 + 2q}f_{\bar{\alpha}}^+(\mathbf{x}_f - \mathbf{e}_{\alpha}\delta_t, t), \quad q \geqslant \frac{1}{2} \qquad (17)$$

where $\mathbf{e}_{\bar{\alpha}}$ is the reversed velocity of $\mathbf{e}_{\alpha}$ ($\mathbf{e}_{\bar{\alpha}} = -\mathbf{e}_{\alpha}$). f_{α}^+ is taken after collision and before propagation. $f_{\bar{\alpha}}(\mathbf{x}_f, t + \delta_t)$ will be used at values after a complete lattice Boltzmann equation time step [31]. Especially, for $q = \frac{1}{2}$, the interpolation formulas reduce to the "bounce-back" scheme. Initially two spherical liquid droplets are placed very close to each other at the center of the complex textured surface which is decorated with conical posts. The conical post height is $H = 15$ in lattice unit (the same unit for the following) and the distance between two consecutive conical posts is $L = 21$. The contact angle between the droplet and the complex textured surface is $\theta = 154°$. Different contact angles can be obtained through adjusting the parameter ρ_w in Eq. (11). Actually, ρ_w is not really relevant to the true density of the solid phase, and it is a free parameter used here to tune different wall properties instead of the true density of solid phase [26]. When the parameter ρ_w varies between ρ_l and ρ_g, the contact angle varies between 0° and 180° [25]. In the following simulations, we set $\theta = 154°$ at $\rho_w = 1.24$. Fig. 5 shows the spontaneous jumping process of the coalesced droplet induced by the coalescence of two droplets with the same radius ($Radius = 35$ in lattice unit). The two droplets are initially placed closely to each other. During the initial period, the liquid bridge between the droplets expands rapidly (from $t = 0$ to $t = 300$) due to the interfacial stress, then the merged droplet forms a dumbbell shape ($t = 500$) followed by elongated capsule shape ($t = 1000$). The detached droplet shows oscillation between the oblate and prolate shapes with rising upward and finally approaches to the spherical shape (from $t = 6000$ to $t = 14,000$). Overall, the released excess surface energy by the coalesced droplet, which dominates over the viscous dissipation and the gravitational potential energy, can induce coalesced droplet spontaneous jumping. Meanwhile, the high pressure which is built up at the bottom contact area provides enough driving force to make the merged
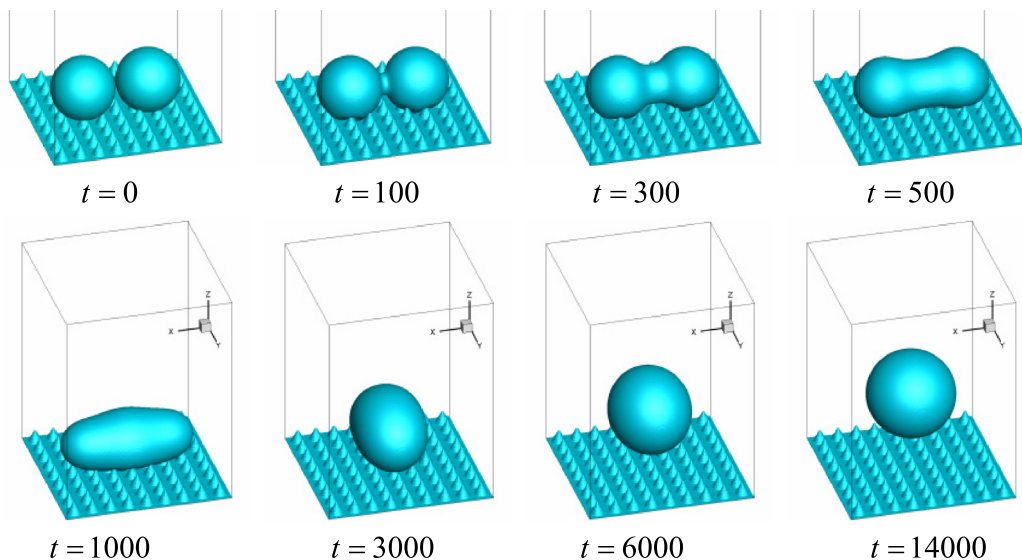

Fig. 5. Time-lapse images of the coalescence-induced droplet jumping on the superhydrophobic surface textured with conical posts. The contact angle between the droplet and the textured surface is $\theta = 154°$.
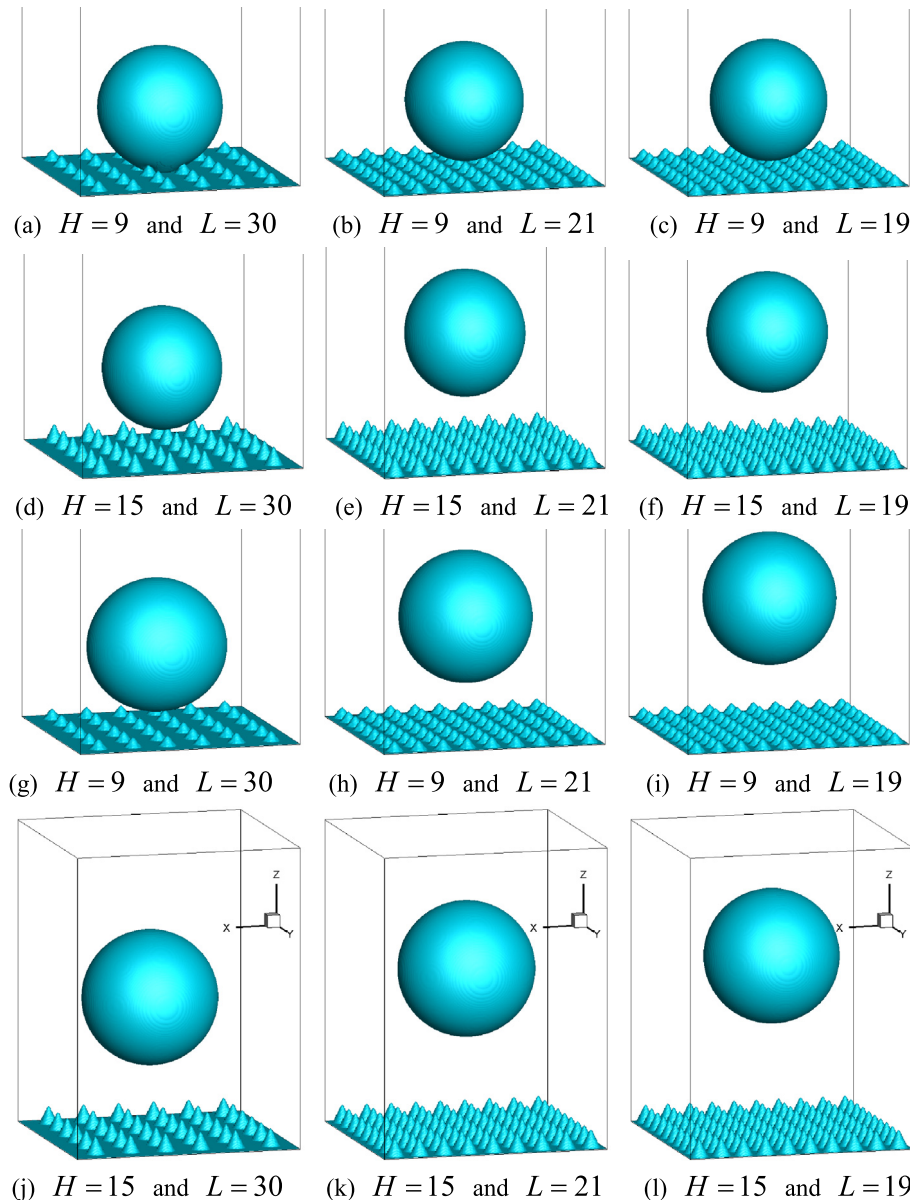
droplet jump spontaneously from the textured surface. This phenomenon was also observed by Nam et al. [4] by the level contour reconstruction method.

4.1.1. Influence of roughness (conical post height and spacing between two consecutive conical posts) on droplet jumping height

Fig. 6 shows the maximum height position of the jumping droplet for different heights of the conical posts and spacing between two consecutive conical posts on a superhydrophobic complex textured surface. The contact angle between the droplet and the complex textured surface is $\theta = 154°$. The initial diameter of the two droplets is *Radius* = 35 for Fig. 6(a)–(f) and *Radius* = 40 for Fig. 6(g)–(l). The conical post heights (H) are 9 and 15, and the spacings between two consecutive conical posts (L) are 30, 21 and 19. From Fig. 6, we find that the coalesced droplet on the conical posts with larger height and small spacing can jump to the highest position (see Fig. 6(f) and (l)). The reason is that the rough textured surface forms a composite solid–liquid–gas interface between the liquid and the surface textured with conical posts. This composite interface exhibits strong liquid repellency due to the gas entrapped among the complex textured surface, hence, the droplet is more likely to jump and reach the highest position on the surface textured with larger height of the posts and smaller spacing between the posts. For the case with lower height of the conical posts and larger spacing between the conical posts, the surface energy that is released upon the coalescence acts to balance the viscous dissipation energy, consequently, there is no energy available for the spontaneous jumping behavior, and the coalesced droplet could not jump from the textured surface in the whole process (see Fig. 6(a)). Meanwhile, we found that the initial two droplets with *Radius* = 40 jumps higher than the initial two droplets with *Radius* = 35. The present result is consistent with the experimental observation reported by Peng et al. [3] and the theoretical analysis by Wang et al. [6]. Fig. 7 shows the jumping height against the time for different complex textured surfaces. Here the initial diameter of the two droplets is *Radius* = 35 corresponding to

(a) $H = 9$ and $L = 30$ (b) $H = 9$ and $L = 21$ (c) $H = 9$ and $L = 19$

(d) $H = 15$ and $L = 30$ (e) $H = 15$ and $L = 21$ (f) $H = 15$ and $L = 19$

(g) $H = 9$ and $L = 30$ (h) $H = 9$ and $L = 21$ (i) $H = 9$ and $L = 19$

(j) $H = 15$ and $L = 30$ (k) $H = 15$ and $L = 21$ (l) $H = 15$ and $L = 19$

Fig. 6. Maximum height position of jumping droplet for different conical post heights (H) and spacings (L) between the conical posts on superhydrophobic textured surface. The contact angle between the droplet and the textured surface is $\theta = 154°$. *Radius* = 35 for (a)–(f) and *Radius* = 40 for (g)–(l).
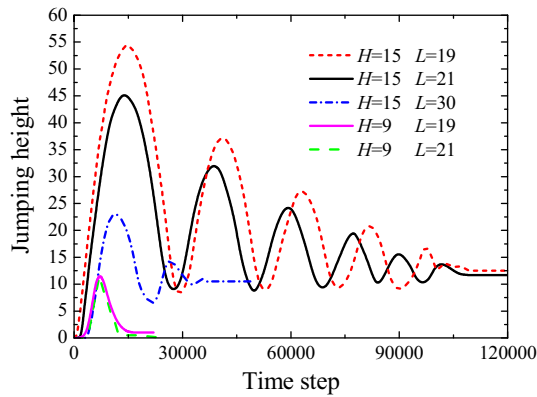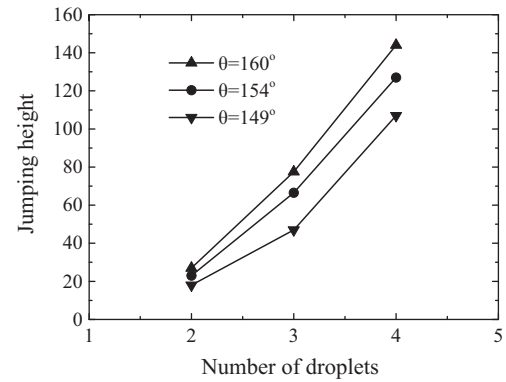
Fig. 7. Jumping height of the coalesced droplet against time step for different textured surfaces.

Fig. 9. Dependence of the droplet jumping height on the number of droplets for different contact angles between the textured surface and the droplet.

Fig. 6(b)–(f) cases. As the time marches, the jumping height shows oscillation and becomes lower and lower. Finally, the coalesced droplet stays still on the complex textured surface. In addition, we find that it is more effective in increasing the height of the conical posts than intensifying the number of the conical posts for inducing spontaneous droplet jumping.
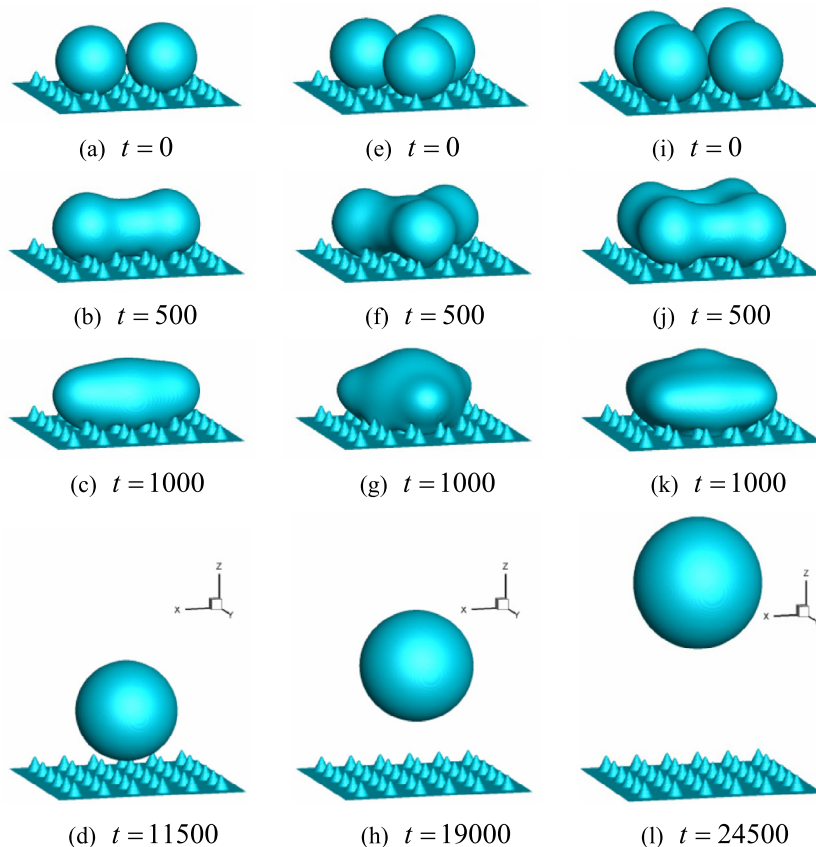
4.1.2. Influence of the number of droplets on droplet jumping height

We set two, three, and four droplets on the complex textured surface to investigate the number of droplets which affects the maximum jumping height of the coalesced droplet. The diameter of the droplets is $Radius = 35$. The height of the conical post is $H = 15$ and the spacing between two consecutive conical posts is $L = 30$. Qualitative analysis of the spontaneous jumping process about two, three, and four droplets are shown in Fig. 8 (see each column of Fig. 8). Since the spontaneous jumping is powered by the excess surface energy released upon droplet coalescence, more droplet coalescence would release more excess surface energy. Therefore, we find that with the increasing of the droplet number, the maximum spontaneous jumping height increases correspondingly (compare Fig. 8(l) with (d)). Fig. 9 shows the jumping height as a function of the number of the droplets for different wettability property of the complex textured surface. From Fig. 9 we find that the spontaneous jumping height becomes higher as the contact

(a) $t = 0$ (e) $t = 0$ (i) $t = 0$

(b) $t = 500$ (f) $t = 500$ (j) $t = 500$

(c) $t = 1000$ (g) $t = 1000$ (k) $t = 1000$

(d) $t = 11500$ (h) $t = 19000$ (l) $t = 24500$

Fig. 8. Time-lapse images of the spontaneous jumping induced by droplet coalescence on textured surface. The contact angle between the textured surface and the droplet is $\theta = 154°$. The initial numbers of droplets are: two droplets for column (a–d), three droplets for column (e–h), and four droplets for column (i–l).

angle between the textured surface and the droplet increases. In other words, more superhydrophobic textured surface is advantageous to inducing higher spontaneous jumping height.

4.1.3. Influence of droplet radius on droplet jumping critical contact angle

The jumping critical contact angle is defined as the required minimal contact angle between the droplet and the complex textured surface which can induce coalesced droplet to jump spontaneously from the textured surface. Two droplets are placed at the center on the textured surface. The conical posts heights (H) are 9 and 15, and the spacings between two consecutive conical posts (L) are 30 and 21. From Fig. 10, we find that the jumping critical contact angle decreases with the increasing radius of the droplet when the droplet radius is smaller than 50, because the large surface tension for large droplet plays dominant role in inducing the coalesced droplet jumping. However, when the radius of the droplet is larger than 50, due to the large contact area with textured surface for a large droplet, the released excess surface energy by the coalesced droplet needs to overcome more viscous dissipation and more surface adhesion than the small coalesced droplet. Therefore, in Fig. 10, the coalescence-induced critical contact angle first decreases to a minimum and then increases when the droplet radius is larger than 50. It indicates that the coalescence-induced bounce velocity decreases gradually with the increasing radius of the droplet under the same surface wettability condition when the droplet radius is larger than 50. In other words, the contact angle between the textured surface and the large droplet should be set large so as to make the coalesced droplet obtain enough velocity to bounce. The present result is consistent with the theoretical analysis by Wang et al. [6], and the experimental observation reported by Boreyko and Chen [1].

4.2. Liquid condensate adhesion on fins in tube-and-fin heat exchanger for different wettability coatings

The tube-and-fin heat exchangers are widely used in a variety of applications like the refrigeration, air-conditioner, humidifier, etc. When the cold surface of the heat exchanger is exposed to air, the liquid condensate occurs on the heat exchanger surface. The formed droplets begin to drain due to the gravity while some droplets adhere to its surface by surface tension. The liquid condensate generated on the surface increases thermal resistance and decreases airflow passage [10]. Consequently, it may decrease the cooling capacity of an air-conditioner and cause flow noise problem as well. The slit fin as one of the enhanced fins, which can enhance heat transfer by renewing the boundary layer and

reducing the thickness of the boundary layer, is widely used to improve the performance of fin-and-tube heat exchangers [32]. Two types of tube-and-fin heat exchangers are tested in this study, including the slit fin and the plain fin. Fig. 11 presents the detailed geometry of one unit in the slit tube-and-fin heat exchanger. The simulation domain is $nx \times ny \times nz = 192 \times 192 \times 256$. The parameters in the lattice unit are fixed at density of liquid $\rho_l = 8.3$, density of gas $\rho_g = 4.15 \times 10^{-2}$, kinematic viscosity for both liquid and gas $\upsilon = 0.136$, surface tension $\sigma = 1.21 \times 10^{-4}$, temperature $T = 4.95 \times 10^{-2}$, and gravitational acceleration $g = 5 \times 10^{-6}$. The no-slip boundary condition is applied on the tube-and-fin surface and bottom surface, and the periodic condition is employed on the others.

Initially, two droplets are placed between the two fins and they contact with the tube. For the reason of the gravity and wettability of the fins, the coalesced droplet falls between the fins. Fig. 12 shows the liquid condensate falling between the fins with and without slits for hydrophilic and hydrophobic coatings. For the plain fin with hydrophilic coating of $\theta = 56°$, the condensate exists on the fin surface in the form of liquid film (see Fig. 12(a) $t = 2100$), and can be drained away easily. For the fin with hydrophobic coating of $\theta = 135°$, the condensate liquid forms a spherical droplet separated from the adjacent fins (see Fig. 12(b) $t = 1200$), and can be drained away immediately as well. After impacting the bottom surface, the droplet resembles a shape of truncated sphere (see Fig. 12(b) $t = 1700$).

The slit fin is advantageous to enhancing heat transfer efficiency, however, the presence of liquid condensate may block the configured fin pattern more easily and thus cause liquid bridge between the fins. The occurrence of liquid condensation that adheres as droplet on the fins may increase the pressure drop and deteriorate the heat transfer performance. Furthermore, the condensation may corrode fins, producing corrosion problem.
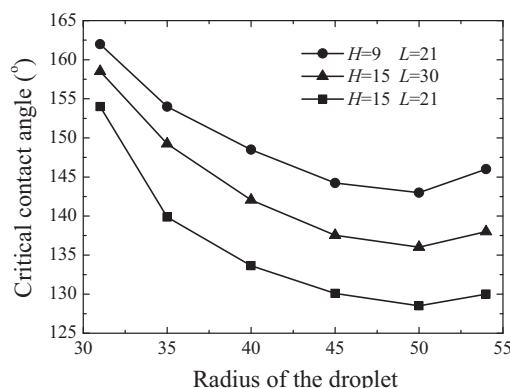

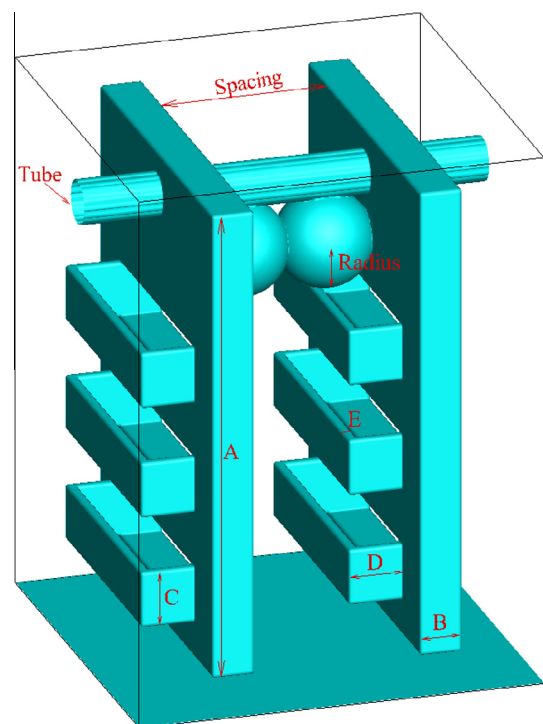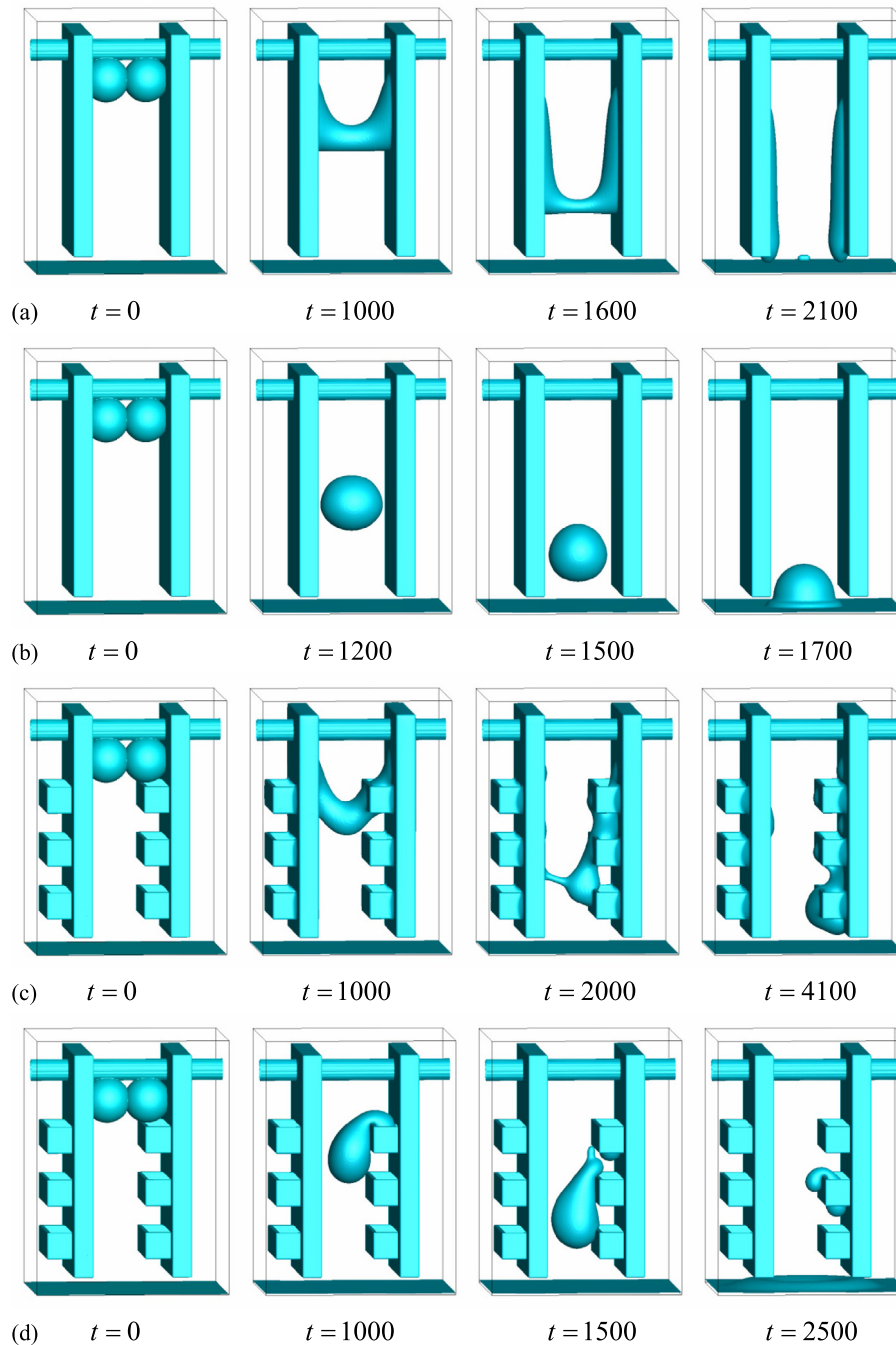Fig. 10. Critical contact angle versus the initial radius of droplet.

Fig. 11. Schematic of the slit fin geometry. Fin length $A = 222$, fin thickness $B = 20$, slit height $C = 25$, slit width $D = 25$, slit thickness $E = 3$, spacing between fins Spacing $= 78$, and droplet radius Radius $= 22$ (all in lattice unit).

Fig. 12. Liquid condensate falls between the fins. (a) Plain fin, $\theta = 56°$, (b) plain fin, $\theta = 135°$, (c) slit fin, $\theta = 38°$, and (d) slit fin, $\theta = 150°$.

Fig. 12 shows the condensate liquid drainage between the slit and plain fin surface with hydrophilic or hydrophobic coatings. Compared to the plain fins, the slit fins are coated with more hydrophilic or more hydrophobic coatings, which are originally more helpful to droplet falling, but we find that it still takes longer time for the liquid condensate to drain on the slit fins (compare Fig. 12(a) with (c), or (b) with (d)). The bulging of the slit fin increases the falling resistance for the droplet. Hence, in order to accelerate the drainage of the droplet between the slit fins, the surface of the slit fins need to be coated with more hydrophilic coating or more hydrophobic coating than the plain fins. From Fig. 12(d), we find that the liquid condensate is more likely to be torn by

the slits, thus the daughter droplet could adhere on the slits. Fig. 13 shows the critical contact angle (for the hydrophilic surfaces, the critical contact angle is defined as the maximum one which can prevent liquid bridge generation between the fins. For the hydrophobic surfaces, the critical contact angle is defined as the minimal one which can prevent liquid bridge generation between the fins) as a function of dimensionless droplet radius for slit and plain fins with hydrophilic and hydrophobic coatings. We find that the slit fin needs to be coated with a lower contact angle for the hydrophilic coating than the plain fin to avoid liquid bridge, while for the hydrophobic coating, the slit fin requires a larger contact angle.
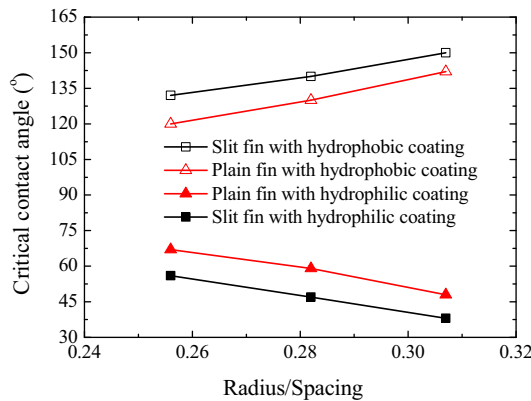
Fig. 13. Critical contact angle as a function of dimensionless droplet radius for slit and plain fins with hydrophobic and hydrophilic coatings.

5. Conclusions

We have investigated the coalescence-induced droplet jumping behavior on superhydrophobic complex textured surface by modifying the wettability of the textured surface, changing the roughness of the textured surface, controlling the number of the droplets as well as the radius of the droplet by the three-dimensional MRT pseudopotential lattice Boltzmann model. The simulation revealed that the coalesced droplet is more likely to jump and reach larger height on the surface textured with larger conical post height and small spacing between the conical posts. With the increasing of the contact angle between the textured surface and the droplet, the jumping height of the coalesced droplet becomes larger. Meanwhile, the maximum spontaneous jumping height increases correspondingly as the number of droplets increases. As the initial radius of droplet increases, the coalescence-induced jumping critical contact angle first decreases to a minimum contact angle and then increases, because the released excess surface energy by a large coalesced droplet needs to overcome more viscous dissipation and more surface adhesion than a small coalesced droplet.

In addition, we have also simulated the liquid condensate adhesion on slit and plain fins in tube-and-fin heat exchanger with hydrophobic and hydrophilic coatings. We found that the hydrophilic coating with small contact angle and the hydrophobic coating with large contact angle are both advantageous to avoiding liquid bridge between the fins. Because the slit fins hinder the droplet from falling, the slit fins should be coated with more hydrophilic coating than the plain fins to avoid liquid bridge. However, for the hydrophobic coating, the slit fins require a larger contact angle than the plain fin to avoid liquid bridge so as to improve the liquid condensate drainage and reduce the pressure drop.

Finally, it should be noted that it is still a challenging work using the multiphase lattice Boltzmann model like Rothman–Keller model, pseudopotential model, free energy model, and mean field model to simulate the multiphase flow with small spurious currents around the interface, maintaining thermodynamic consistency, at large density ratio and large viscosity ratio. The robustness and stability of the pseudopotential model still need to be improved, especially when it is applied to large density ratio, large viscosity ratio and high Reynolds number. In the present simulations, the curved solid boundary of the conical posts leads to more serious numerical instability as well. It is urgent to improve the multiphase lattice Boltzmann model or develop new stable computing scheme for solving the Navier–Stokes equations, which can be recovered by the multiphase lattice Boltzmann model, so as to achieve numerical stability and simulate complicated cases more close to the real physics.

References

[1] J.B. Boreyko, C.H. Chen, Self-propelled dropwise condensate on superhydrophobic surfaces, Phys. Rev. Lett. 103 (2009) 184501.
[2] N. Miljkovic, R. Enright, Y. Nam, K. Lopez, N. Dou, J. Sack, E.N. Wang, Jumping-droplet-enhanced condensation on scalable superhydrophobic nanostructured surfaces, Nano Lett. 13 (2013) 179–187.
[3] B.L. Peng, S.F. Wang, Z. Lan, W. Xu, R.F. Wen, X.H. Ma, Analysis of droplet jumping phenomenon with lattice Boltzmann simulation of droplet coalescence, Appl. Phys. Lett. 102 (2013) 151601.
[4] Y. Nam, H. Kim, S. Shin, Energy and hydrodynamic analyses of coalescence-induced jumping droplets, Appl. Phys. Lett. 103 (2013) 161601.
[5] X.L. Liu, P. Cheng, X.J. Quan, Lattice Boltzmann simulations for self-propelled jumping of droplets after coalescence on a superhydrophobic surface, Int. J. Heat Mass Transfer 73 (2014) 195–200.
[6] F.C. Wang, F.Q. Yang, Y.P. Zhao, Size effect on the coalescence-induced self-propelled droplet, Appl. Phys. Lett. 98 (2011) 053112.
[7] C.C. Wang, C.T. Chang, Heat and mass transfer for plate fin-and-tube heat exchangers, with and without hydrophilic coating, Int. J. Heat Mass Transfer 41 (1998) 3109–3120.
[8] A.D. Sommers, R. Yu, N.C. Okamoto, K. Upadhyayula, Condensate drainage performance of a plain fin-and-tube heat exchanger constructed from anisotropic micro-grooved fins, Int. J. Refrig. 35 (2012) 1766–1778.
[9] Z.G. Guo, F. Zhou, J.C. Hao, W.M. Liu, Effect of system parameters on making aluminum alloy lotus, J. Colloid Interface Sci. 303 (2006) 298–305.
[10] J.M. Shin, S. Ha, The effect of hydrophilicity on condensation over various types of fin-and-tube heat exchangers, Int. J. Refrig. 25 (2002) 688–694.
[11] J.J. Huang, C. Shu, Y.T. Chew, Numerical investigation of transporting droplets by spatiotemporally controlling substrate wettability, J. Colloid Interface Sci. 328 (2008) 124–133.
[12] H.H. Liu, Y.H. Zhang, Droplet formation in a T-shaped microfluidic junction, J. Appl. Phys. 106 (2009) 034906.
[13] S. Alapati, S.M. Kang, Y.K. Suh, Parallel computation of two-phase flow in a microchannel using the lattice Boltzmann method, J. Mech. Sci. Technol. 23 (2009) 2492–2501.
[14] Q.J. Kang, D.X. Zhang, S.Y. Chen, X.Y. He, Lattice Boltzmann simulation of chemical dissolution in porous media, Phys. Rev. E 65 (2002) 036318.
[15] G.G. Le, J.F. Zhang, Boundary slip from the immersed boundary lattice Boltzmann models, Phys. Rev. E 79 (2009) 026701.
[16] S. Chibbaro, L. Biferale, F. Diotallevi, S. Succi, Capillary filling for multicomponent fluid using the pseudo-potential lattice Boltzmann method, Eur. Phys. J. 171 (2009) 223–228.
[17] P. Yuan, L. Schaefer, Equations of state in a lattice Boltzmann model, Phys. Fluids 18 (2006) 042101.
[18] X.W. Shan, Analysis and reduction of the spurious current in a class of multiphase lattice Boltzmann models, Phys. Rev. E 73 (2006) 047701.
[19] M. Sbragaglia, R. Benzi, L. Biferale, S. Succi, K. Sugiyama, F. Toschi, Generalized lattice Boltzmann method with multirange pseudopotential, Phys. Rev. E 75 (2007) 026702.
[20] Q. Li, K.H. Luo, X.J. Li, Lattice Boltzmann modeling of multiphase flows at large density ratio with an improved pseudopotential model, Phys. Rev. E 87 (2013) 053301.
[21] P. Lallemand, L.S. Luo, Theory of the lattice Boltzmann method: dispersion, dissipation, isotropy, Galilean invariance, and stability, Phys. Rev. E 61 (2000) 6546–6562.
[22] M.E. McCracken, J. Abraham, Multiple-relaxation-time lattice-Boltzmann model for multiphase flow, Phys. Rev. E 71 (2005) 036701.
[23] D. Zhang, K. Papadikis, S. Gu, Three-dimensional multi-relaxation time lattice-Boltzmann model for the drop impact on a dry surface at large density ratio, Int. J. Multiphase Flow 64 (2014) 11–18.
[24] N.S. Martys, H.D. Chen, Simulation of multicomponent fluids in complex three-dimensional geometries by the lattice Boltzmann method, Phys. Rev. E 53 (1996) 743–750.
[25] H.B. Huang, Z.T. Li, S.S. Liu, X.Y. Lu, Shan-and-Chen-type multiphase lattice Boltzmann study of viscous coupling effects for two-phase flow in porous media, Int. J. Numer. Methods Fluids 61 (2009) 341–354.
[26] R. Benzi, L. Biferale, M. Sbragaglia, S. Succi, F. Toschi, Mesoscopic modeling of a two-phase flow in the presence of boundaries: the contact angle, Phys. Rev. E 74 (2006) 021509.

[27] S. Gong, P. Cheng, A lattice Boltzmann method for simulation of liquid–vapor phase-change heat transfer, Int. J. Heat Mass Transfer 55 (2012) 4923–4927.

[28] X.L. Liu, P. Cheng, Lattice Boltzmann simulation of steady laminar film condensation on a vertical hydrophilic subcooled flat plate, Int. J. Heat Mass Transfer 62 (2013) 507–514.

[29] A.H. Harvey, A.P. Peskin, S.A. Klien, NIST/ASME Steam Properties, Version 2.21. National Institute of Standards and Technology, US, 2004.

[30] K.N. Premnath, J. Abraham, Three-dimensional multi-relaxation time (MRT) lattice-Boltzmann models for multiphase flow, J. Comput. Phys. 224 (2007) 539–559.

[31] M. Bouzidi, M. Firdaouss, P. Lallemand, Momentum transfer of a Boltzmann-lattice fluid with boundaries, Phys. Fluids 13 (2001) 3452–3459.

[32] X.K. Ma, G.L. Ding, Y.M. Zhang, K.J. Wang, Airside heat transfer and friction characteristics for enhanced fin-and-tube heat exchanger with hydrophilic coating under wet conditions, Int. J. Refrig. 30 (2007) 1153–1167.